



ELSEVIER

Contents lists available at ScienceDirect

## International Journal of Mechanical Sciences

journal homepage: [www.elsevier.com/locate/ijmecsci](http://www.elsevier.com/locate/ijmecsci)

# Tunable permittivity in dielectric elastomer composites under finite strains: Periodicity, randomness, and instabilities.

Artemii Goshkoderia<sup>a</sup>, Nitesh Arora<sup>b</sup>, Viacheslav Slesarenko<sup>c,d</sup>, Jian Li<sup>e</sup>, Vincent Chen<sup>f,g</sup>, Abigail Juhl<sup>g</sup>, Philip Buskohl<sup>g</sup>, Stephan Rudykh<sup>b,\*</sup>

<sup>a</sup> Department of Aerospace Engineering, Technion – Israel Institute of Technology, Haifa 32000, Israel

<sup>b</sup> Department of Mechanical Engineering, University of Wisconsin – Madison, Madison, WI 53706, USA

<sup>c</sup> Freiburg Institute for Advanced Studies, Freiburg im Breisgau, Germany 79104

<sup>d</sup> Cluster of Excellence livMatS @ FIT, University of Freiburg, Freiburg im Breisgau, Germany 79110

<sup>e</sup> Department of Civil & Environmental Engineering, Massachusetts Institute of Technology, Cambridge, MA 02138, USA

<sup>f</sup> UES, Inc., Dayton, OH 45432, USA

<sup>g</sup> Air Force Research Laboratory, Wright-Patterson AFB, OH 45433-7718, USA

## ARTICLE INFO

## Keywords:

Dielectric elastomers  
Effective permittivity  
Microstructure  
Soft materials

## ABSTRACT

We study the interplay between the material composition and deformation in dielectric elastomer (DE) composites with periodically and randomly distributed particles embedded in a soft matrix. We focus on the deformation-induced tunability of the effective permittivity in DE composites. We examine the effects of microstructural periodicity and its transition towards random distribution. In particular, we analyze the DE composites with periodic microstructures of (a) circular and (b) elliptical inclusions, (c) pair of inclusions, and (d) randomly distributed inclusions with different numbers of the particles in the unit cell. The finitely deformed DE composites with ideal dielectric elastomer constituents are analyzed numerically. In addition, for the periodic DE composites with circular inclusions, we derive an explicit relation between the effective permittivity and stretch. The effective permittivity of DE composites with periodic microstructures changes with deformation, whereas in DE composites with randomly distributed inclusions, the permittivity is barely affected by deformation. For the latter case, the effective permittivity attains a certain value as the number of particles in the periodic cell increases. To provide the insights on the composite behavior, a two-particle periodic system is examined. The permittivity is found to be sensitive to the orientation of the pairs with respect to the applied electric field, and the distance between the particles. The geometrical effects amplify significantly as the inter-particle distance becomes less than their two diameters. Finally, we illustrate the permittivity tunability in DE periodic porous composites structures experiencing elastic instabilities.

## 1. Introduction

Dielectric elastomers (DEs) can generate large deformations when excited by an electric field [1–4]. DEs have attracted significant attention in view of potential applications such as artificial muscles [5], energy-harvesting and noise canceling devices, soft robotics [6–9], tunable waveguides [10–14] and soft display [15], to name a few. However, practical implementation of the DE technologies is limited due to the high electric fields required for exerting large strains. The weak electromechanical coupling can be potentially improved through the usage of heterogeneous DEs combining soft elastomers with high-dielectric-constant stiff materials [16–19]; the active materials include ceramic powders such as TiO<sub>2</sub> particles [20,21], BaTiO<sub>3</sub> nanoparticles [22] and PbTiO<sub>3</sub> particles [23]. However, the mechanical rein-

forcement of the stiff inclusions increases the overall stiffness of DE composites and, thus, reduces the electromechanical coupling. To overcome this issue, neat microstructures need to be designed [24]. This required the development of theoretical modeling [25–27] and numerical approaches [28,29]. The subsequent theoretical studies and numerical simulations [24,30] predicted significant enhancements in the performance of DE composites with periodic microstructures. Improvement by orders of magnitude in the electromechanical coupling can be achieved using a hierarchically structured composites comprising softer and stiffer phases [24,31] or even by utilizing electromechanical instabilities [32,33], and modulating the input waveform [34]. To realize the designed microstructures, advanced material fabrication techniques can be used. Recent advances in the material fabrication and 3D printing, allowing realization of highly structured materials at different length-scales [35–37], provide a great perspective for enhancing DE performance through microstructure. Additional suitable material fabrication techniques includes filling the DE with multi-walled carbon nan-

\* Corresponding author.

E-mail address: [rudykh@wisc.edu](mailto:rudykh@wisc.edu) (S. Rudykh).

otubes [38], embedding of glycerol in PDMS [39] and grafting of copper phthalocyanine oligomer onto an acrylic elastomer backbone [40]. We note the experimental studies indicate significant enhancements in the electromechanical coupling [17,41].

Motivated by experimental studies [42,43], statistical mechanics of a Gaussian polymer chains have been employed to construct models reproducing the dependence of the dielectric permittivity of an elastomer on the applied deformation [44–46]. Moreover, the effect of deformation on the effective permittivity of periodic DE composites could be used to achieve tunable effective permittivity. This property tunability can have potential applications in a variety of smart materials and structures such as deformable antennas [47–49], electromagnetic smart screens [50] and sensors [51–53].

In this study, we analyze the effects of the periodic microstructure and deformation on the tunability of the effective permittivity in DE composites. We examine the DE composites with ideal dielectric elastomer constitutions by means of finite element simulations. We consider two-phase heterogeneous DE composites consisting of a rubber-like matrix and stiff circular or elliptical electroactive particles. We investigate several microstructures with square initial periodicity: (a) single circular and (b) elliptical inclusions, (c) pair of inclusions, and (d) randomly distributed inclusions with varying number of the particles in the unit cell. We analyze the effects of particles shape, microstructure geometrical parameters, and material properties on the effective permittivity of the DE composites. In addition, for the periodic DE composites with rigid circular inclusions, we derive an explicit relation between the effective permittivity and stretch based on the Maxwell-Garnett mixing rule for multiphase composites.

Finally, we explore the permittivity tunability in soft materials experiencing a local buckling leading to pre-designed dramatic microstructure transformations [54,55]. In particular, we consider soft materials with periodically distributed voids in a square arrangement [54], and voids combined with inclusions in a rectangular arrangement [56–58]. Upon achieving the critical strain, the voids collapse in a collaborative manner giving rise to their new doubled periodicity and pronounced auxetic behavior. Here, we illustrate that the instability-driven geometrical changes can be used for tunability in the effective permittivity.

## 2. Theoretical Background

We denote by  $\Omega_0$  and  $\Omega$  the regions occupied by a body in the reference and current configurations, respectively. The Cartesian position vector of a material point in the reference configuration of a body is  $\mathbf{X}$  and its position vector in the deformed configuration is  $\mathbf{x}$ . We introduce a mapping vector function  $\boldsymbol{\chi}$  such that

$$\mathbf{x} = \boldsymbol{\chi}(\mathbf{X}). \quad (1)$$

The deformation gradient is defined as

$$\mathbf{F} = \frac{\partial \boldsymbol{\chi}(\mathbf{X})}{\partial \mathbf{X}}. \quad (2)$$

The ratio between the volumes in the current and reference configurations is  $J \equiv \det \mathbf{F} > 0$ .

We consider a quasi-static deformation in the absence of a magnetic field, electrical charges or electric currents within the material. Consequently, Maxwell equations take the form

$$\text{Div} \mathbf{D}^0 = 0 \quad \text{and} \quad \text{Curl} \mathbf{E}^0 = \mathbf{0}, \quad (3)$$

where  $\mathbf{D}^0$  is the electric displacement and  $\mathbf{E}^0$  is the electric field in the reference configuration and  $\text{Div}(\bullet)$  and  $\text{Curl}(\bullet)$  are the differential operators with respect to  $\mathbf{X}$ . The referential electric field and electric displacement are related to their counterpart in the deformed configuration [27,59] via

$$\mathbf{E}^0 = \mathbf{F}^T \mathbf{E} \quad \text{and} \quad \mathbf{D}^0 = J \mathbf{F}^{-1} \mathbf{D}. \quad (4)$$

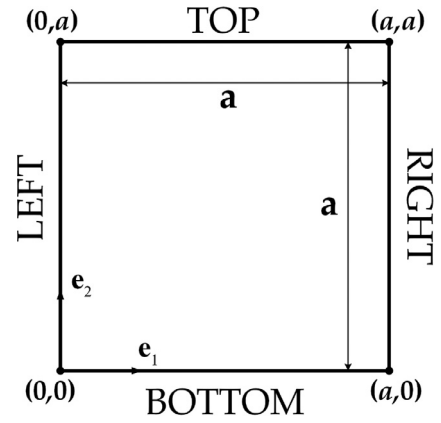


Fig. 1. Schematic representation of a square unit cell in the two-dimensional space. The periodic boundary conditions are applied on the four sides of the unit cell.

We follow the analysis proposed by Dorfmann and Ogden [27,59] and consider the elastic dielectrics whose constitutive relation is given in terms of a scalar-valued energy-density function  $\Psi(\mathbf{F}, \mathbf{E}^0)$  such that

$$\mathbf{P} = \frac{\partial \Psi(\mathbf{F}, \mathbf{E}^0)}{\partial \mathbf{F}} \quad \text{and} \quad \mathbf{D}^0 = - \frac{\partial \Psi(\mathbf{F}, \mathbf{E}^0)}{\partial \mathbf{E}^0}, \quad (5)$$

where  $\mathbf{P}$  is the total nominal stress tensor.

## 3. Analysis

In this section, we consider DE composite that occupies a domain  $\Omega_0$  (in the undeformed configuration), which is made of two distributed (homogeneous) phases, occupying subdomains  $\Omega_0^{(r)}$  ( $r = 1, 2$ ) in  $\Omega_0$ . The energy-density function of a two-phase composite is

$$\Psi(\bar{\mathbf{F}}, \mathbf{X}, \bar{\mathbf{E}}^0) = \varphi^{(1)}(\mathbf{X}) \Psi^{(1)}(\mathbf{F}, \mathbf{E}) + \varphi^{(2)}(\mathbf{X}) \Psi^{(2)}(\mathbf{F}, \mathbf{E}), \quad (6)$$

where the characteristic function defined in each phase  $r$  is

$$\varphi^{(r)}(\mathbf{X}) = \begin{cases} 1, & \text{if } \mathbf{X} \in \Omega_0^{(r)}; \\ 0, & \text{otherwise.} \end{cases} \quad (7)$$

The volume fraction of the  $r$ -phase is

$$c^{(r)} = \frac{1}{V} \int_{\Omega_0} \varphi^{(r)}(\mathbf{X}) dV, \quad (8)$$

where  $V$  is the total volume of the domain  $\Omega_0$ . The volume fractions are related via

$$c^{(1)} + c^{(2)} = 1. \quad (9)$$

In our finite element simulations, the macroscopic electro-mechanical loading is implemented by applying periodic boundary conditions for both displacement and electric field. The applied average deformation gradient and electric field together with electric displacement are

$$\bar{\mathbf{F}} = \frac{1}{V} \int_{\Omega_0} \mathbf{F}(\mathbf{X}) dV, \quad \bar{\mathbf{D}}^0 = \frac{1}{V} \int_{\Omega_0} \mathbf{D}^0(\mathbf{X}) dV \quad \text{and} \quad \bar{\mathbf{E}}^0 = \frac{1}{V} \int_{\Omega_0} \mathbf{E}^0(\mathbf{X}) dV, \quad (10)$$

respectively. Here, we restrict our attention to a 2-D setting, where the integration is performed over the area of a periodic unit cell occupying the domain

$$0 \leq X_1 \leq a \quad \text{and} \quad 0 \leq X_2 \leq a, \quad (11)$$

in the reference configuration (see Fig. 1). The periodic boundary conditions are:

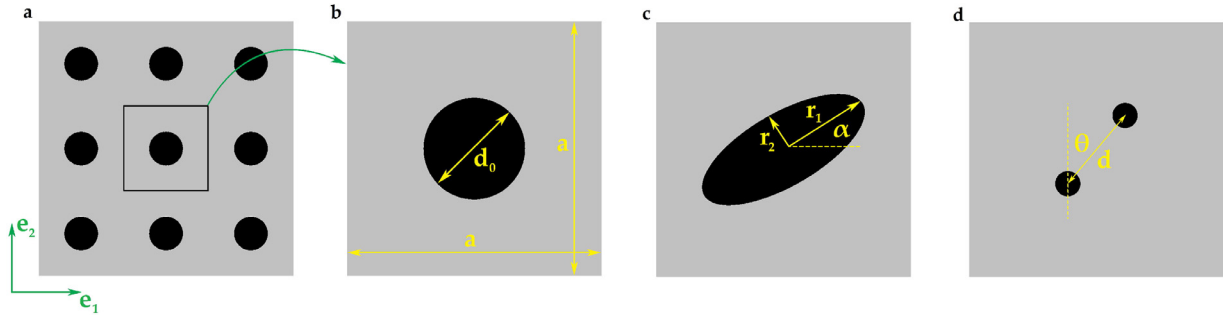


Fig. 2. A schematic representation of DE composites with square periodic microstructures (a), with black regions denoting stiff, high permittivity inclusions of (b) circular, (c) elliptical and (d) a pair of equi-sized circular shapes.

The top ( $X_2 = a$ ) and bottom ( $X_2 = 0$ ) sides are related via

$$\begin{cases} u_2^B = u_2^T + (\bar{F}_{22} - 1)a, \\ u_1^B = u_1^T, \\ U^B(X_1, 0) = U^T(X_1, a) + \bar{E}_2^0 a. \end{cases} \quad (12)$$

The right ( $X_1 = a$ ) and left ( $X_1 = 0$ ) sides are related via

$$\begin{cases} u_1^L = u_1^R + (\bar{F}_{11} - 1)a, \\ u_2^L = u_2^R, \\ U^L(0, X_2) = U^R(a, X_2), \end{cases} \quad (13)$$

where  $U = -\text{grad } \mathbf{E}$  is the electric potential. Superscripts  $B$ ,  $T$ ,  $L$ ,  $R$  are abbreviations of ‘Bottom’, ‘Top’, ‘Left’ and ‘Right’, respectively (see Fig. 1).

The application of the periodic boundary conditions allows us to determine the solution along the electro-mechanical loading path, defined as

$$\bar{\mathbf{F}} = \lambda \mathbf{e}_1 \otimes \mathbf{e}_1 + \lambda^{-1} \mathbf{e}_2 \otimes \mathbf{e}_2 + \mathbf{e}_3 \otimes \mathbf{e}_3 \quad \text{and} \quad \bar{\mathbf{E}}^0 = \bar{E}_2^0 \mathbf{e}_2. \quad (14)$$

Note that we consider the electric field applied in the direction of  $\mathbf{e}_2$ . The analysis is implemented in the finite element code COMSOL Multiphysics. To ensure the accuracy of the numerical results, a mesh sensitivity analysis was performed; the details and illustrative results can be found in Appendix A.

## 4. Results

### 4.1. Two-phase composites

We consider DE composites with phases described by an ideal dielectric elastomer model, in particular, the following energy-density function is used

$$\Psi^{(r)}(\mathbf{F}, \mathbf{E}^0) = \frac{\mu^{(r)}}{2} (\text{Tr} \mathbf{C} - 3) - \frac{\varepsilon_0 \varepsilon^{(r)} J}{2} \mathbf{E}^0 \mathbf{C}^{-1} \mathbf{E}^0 - \mu^{(r)} \ln J + \frac{\Lambda^{(r)}}{2} (J - 1)^2, \quad (15)$$

where  $\mu$  is the shear modulus and  $\Lambda$  is the Lamé’s first parameter,  $\varepsilon_0$  is the vacuum permittivity,  $\varepsilon^{(r)}$  is the relative permittivity, and  $\mathbf{C} = \mathbf{F}^T \mathbf{F}$  is the right Cauchy-Green tensor. Throughout the text, the superscripts  $(\bullet)^{(m)}$  and  $(\bullet)^{(i)}$  are used to denote the quantities of matrix and inclusion phases, respectively. In the numerical analysis, a nearly incompressible phase behavior is maintained by assigning a high ratio between the first Lamé parameter and shear modulus, namely,  $\Lambda^{(r)}/\mu^{(r)} = 100$ . Note that while the macroscopic deformation is enforced to be incompressible, locally, the phases are allowed to develop some compressible (nearly incompressible) deformations. The contrasts in the shear moduli and relative permittivities are defined as  $k_\mu = \mu^{(i)}/\mu^{(m)}$  and  $k_\varepsilon = \varepsilon^{(i)}/\varepsilon^{(m)}$ . The shear modulus and relative permittivity of the matrix are taken to be  $\mu^{(m)} = 1$  MPa and  $\varepsilon^{(m)} = 5$ . A schematic representation of the unit cells is given in Fig. 2.

The components of the effective permittivity tensor can be found from the following relation

$$\varepsilon_0 \bar{\varepsilon}_{ij} \bar{E}_j = \bar{D}_i, \quad (16)$$

where  $\bar{\mathbf{D}}$  and  $\bar{\mathbf{E}}$  are the average electric displacement and electric field, respectively (the average is over the unit cell area in the current configuration). In realistic situations (e.g., thin film dielectric elastomer actuators), one may be interested in prescribing only the component  $\bar{\varepsilon}_2 = \bar{\varepsilon}_{22}$ . This component represents the effective permittivity of the composite in the direction of the applied electric field typically produced by two compliant electrodes attached to the faces of a thin film elastomer. We note that in our analysis we apply a relatively low electric field so that the potential induced microstructure distortion is negligible. In particular, the level of the applied test (normalized) electric field is  $\bar{E}_2^0 = E_2^0 / \sqrt{\mu^{(m)}/(\varepsilon_0 \varepsilon_{22}^{(m)})} = 0.05$  results in the strain level less than 0.01% in homogeneous materials. Then, by using Eq. (16), we evaluate the effective permittivity along the electromechanical loading path defined by Eq. (14).

#### 4.1.1. Circular inclusion

First we consider the DE composites with periodically distributed circular inclusions with a 2-D periodic unit cell with circular inclusions illustrated in Fig. 2(a,b). The effective permittivity for the periodic DE composites with circular inclusions can be estimated as [60–62]

$$\varepsilon_2^* = \frac{k_\varepsilon + 1 + c(k_\varepsilon - 1)}{k_\varepsilon + 1 - c(k_\varepsilon - 1)}, \quad (17)$$

where  $(\bullet)^*$  denotes the normalized value  $(\bullet)/\varepsilon^{(m)}$  and  $c$  is the volume fraction of the inclusion phase. Eq. (17) is also known as lower Hashin-Shtrikman bound.

However, the composite microstructure evolves as finite strains are applied. As a result, the effective permittivity is affected by the deformation. The effect of the applied strain on the effective permittivity of the deformed unit cell can be estimated as follows. Recall that the DE composite can be considered as an electric capacitor. Here, we consider the unit cell of DE composite as a capacitor or an assembly of capacitors with the corresponding circuit diagrams shown in Fig. 3. Once the total capacitance of the deformed unit cell is known, its effective permittivity can be evaluated directly. To evaluate the total capacitance, we divide the deformed unit cell into three sub-domains such that their permittivities are known and their capacitances can be readily evaluated. The deformed sub-domains are (1) single central square unit cell of the DE composite and (2) two rectangles. The central sub-domain (1) has the side length  $a/\lambda$  for  $\lambda > 1$  (area labeled as “1” in Fig. 3(b)) or  $a\lambda$  for  $\lambda < 1$  (area labeled as “1” in Fig. 3(c)). The two rectangles have their side lengths  $[a(\lambda^2 - 1)/2\lambda, a/\lambda]$  for  $\lambda > 1$  and  $[a(1 - \lambda^2)/2\lambda, a\lambda]$  for  $\lambda < 1$  (shaded areas labelled as “2”). The permittivity of the shaded rectangles is  $\varepsilon_2 = \varepsilon^{(m)}$ . For the square composite unit cell (1), the permittivity is given by using Eq. (17) with the updated volume fraction,  $c_{\text{updated}} = c\lambda^2$  for  $\lambda > 1$  and  $c_{\text{updated}} = c/\lambda^2$  for  $\lambda < 1$ . The capacitance of each sub-domain is calculated using their respective dimensions and permittivity.

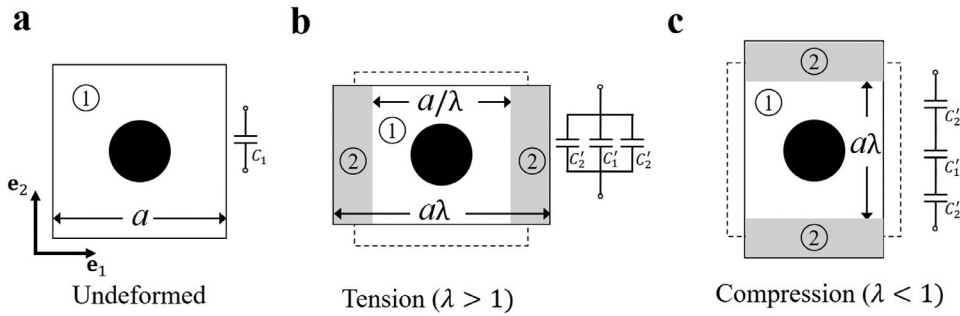


**Fig. 3.** Schematic representation of the periodic DE composite square unit cell with circular inclusions: (a) undeformed; (b) under tension ( $\lambda > 1$ ), approximated as assembly of capacitors in parallel; and (c) under compression ( $\lambda < 1$ ), approximated as assembly of capacitors in series.

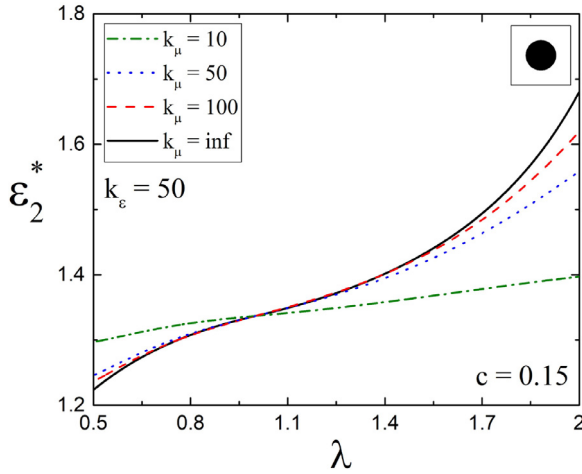


**Fig. 4.** Effective permittivity vs stretch for periodic DE composite with a circular inclusion. The volume fraction of the inclusion is  $c = 0.15$ . The permittivity contrast is  $k_\epsilon = 50$ . Green dash-dotted, blue dotted, and red dashed curves correspond to the DE composites with shear moduli contrast  $k_\mu = 10, 50$  and  $100$ , respectively; the black continuous curve corresponds to the analytical results derived for the case of rigid inclusion  $k_\mu = \infty$ .

Next, we calculate the total capacitance of the deformed unit cell using the assembly formulation for capacitors. Specifically, for  $\lambda > 1$ , the three capacitors,  $C'_2$  (shaded rectangular sub-domain),  $C'_1$  (composite square sub-domain), and  $C'_2$  are assembled in their parallel configuration (see Fig. 3(b)). For  $\lambda < 1$ , the capacitors  $C''_2$ ,  $C''_1$ , and  $C''_2$  are assembled in series (see Fig. 3(c)). Finally, using the total capacitance, we obtain the effective permittivity of the deformed DE composite as

$$\epsilon_2^*(\lambda) = \begin{cases} \frac{\lambda^2(k_\epsilon + 1) + c(k_\epsilon - 1)}{\lambda^2(k_\epsilon + 1) + c(1 - 2\lambda^2)(k_\epsilon - 1)}, & \text{if } \lambda \leq 1; \\ \frac{k_\epsilon + 1 + c(2 - \lambda^2)(k_\epsilon - 1)}{k_\epsilon + 1 - c\lambda^2(k_\epsilon - 1)}, & \text{if } \lambda \geq 1. \end{cases} \quad (18)$$

Fig. 4 shows the dependence of the normalized effective permittivity on the stretch ratio. The results are shown for the DE composites with the shear moduli contrasts  $k_\mu = 10$  (olive dash-dotted curve),  $k_\mu = 50$  (blue dotted curve),  $k_\mu = 100$  (red dashed curve). The black continuous curve denotes the predictions of the analytical expression given by Eq. (18) for the rigid inclusion case  $k_\mu = \infty$ . We observe that  $\epsilon_2^*(\lambda)$  is a monotonically increasing function of  $\lambda$  for every value of the contrast  $k_\mu$ , with the lowest and the highest values  $\epsilon_{\min, \lambda=0.5}$  and  $\epsilon_{\min, \lambda=2}$ , respectively. We define the tunability of the effective permittivity as  $\Delta_\epsilon = (\epsilon_{\max} - \epsilon_{\min})/\epsilon_{\min}$ . The tunability is higher in DE composites with high shear modulus contrast. For example, for  $k_\mu = 100$ , the value  $\Delta_\epsilon = [(\epsilon_{\max}(\lambda = 2) - \epsilon_{\min}(\lambda = 0.5))/\epsilon_{\min}(\lambda = 0.5)] \cdot 100\% = 31\%$ . For this case of a relatively stiff inclusion ( $k_\mu = 100$ ), the deformation of the inclusion is small, and the inclusion shape does not change significantly with the

applied deformation. We note that the simulation results for  $k_\mu = 100$  are in good agreement with the analytical estimate for the stretches  $0.6 \lesssim \lambda \lesssim 1.6$ . However, for larger deformations  $\lambda \lesssim 0.6$  and  $\lambda \gtrsim 1.6$  the change of the inclusion shape becomes significant and the dashed curve ( $k_\mu = 100$ ) branches out from the continuous curve (corresponding to rigid inclusion). An increase in the shear modulus contrast leads to a decrease in  $\epsilon_2^*$  for  $\lambda < 1$  and increase for  $\lambda > 1$ . As expected, all the curves intersect at the point corresponding to the undeformed state ( $\lambda = 1$  and  $\epsilon_2^* = 1.34$ ). Note that the distance between the curves increases rapidly with the applied deformation for  $\lambda > 1$ . Therefore, it is possible to tune the effective permittivity of DE composites by *pre-stretch*. Moreover, the effective permittivity can be tuned by DE composition; thus, for instance, Eq. (18) predicts the minimum permittivity  $\epsilon_{\min}(\lambda = 0.5) = 1.24$  in the composite with volume fraction  $c = 0.11$ , and the maximum  $\epsilon_{\max}(\lambda = 2) = 1.62$  in the composite with  $c = 0.25$ .

#### 4.1.2. Elliptical inclusion

Next, we consider the periodic DE composites with elliptical inclusions with their corresponding unit cell shown in Fig. 2(c). The aspect ratio of the elliptical particles is defined as the ratio between the semi-major and the semi-minor axes, namely,  $w = r_1/r_2$ . The inclusion inclination angle  $\alpha$  is defined as the angle between  $\mathbf{e}_1$ -direction and semi-major axis of the elliptical inclusions. Due to the symmetry of the unit cell, only inclination angles in the range  $0 \leq \alpha \leq \pi/2$  are considered.

The dependence of the normalized effective permittivity on the applied stretch for DE composites with the shear moduli contrasts  $k_\mu = 10$  (black dashed curve),  $50$  (blue continuous curve) and  $100$  (red dash-dotted curve) is shown in Fig. 5(a). We observe that for the compressive range of deformation,  $\lambda < 1$ , the curves have their own maximum. The largest value of  $\epsilon_2^* = 1.41$  corresponds to the  $k_\mu = 10$  (dashed curve). An increase in the shear modulus contrast results in a decrease in the effective permittivity for compression ( $\lambda < 1$ ), and in an increase for tension ( $\lambda > 1$ ) for any stretch ratio. For tension ( $\lambda > 1$ ), we observe that the dash-dotted ( $k_\mu = 100$ ) and continuous ( $k_\mu = 50$ ) curves have their minimum, whereas the dashed curve (corresponding to the soft DE composite  $k_\mu = 10$ ) flattens with an increase in stretch ratio.

The dependence of the normalized effective permittivity on the applied stretch for inclusion inclination angles  $\alpha = 0$  (black dashed curve),  $\alpha = \pi/4$  (blue continuous curve) and  $\alpha = \pi/2$  (red dash-dotted curve) is shown in Fig. 5(b). The dependence is almost linear for the DE composite with inclination angle  $\alpha = 0$ . An increase in the inclination angle leads to an increase in the value of  $\epsilon_2^*$ . We observe that the rate of change in permittivity with respect to  $\lambda$  increases as the angle increases from  $0$  to  $\pi/2$ . For the cases of  $\alpha = 0$  and  $\alpha = \pi/2$ , the effective permittivity increases with applied deformation for  $\lambda > 1$  and decreases for  $\lambda < 1$ . The opposite effect is observed in the DE composite with the initial inclination angle  $\alpha = \pi/4$ . In this case,  $\epsilon_2^*(\lambda)$  monotonically increases as the stretch ratio is increased. We observe that the highest (lowest) effective permittivity is reached when the orientation of the major (minor) semi-axis of the elliptical inclusion coincides with the direction of the applied electric field. Finally, we note that for the DE composite considered in Fig. 5(b), the tunability of effective permittivity provided by change

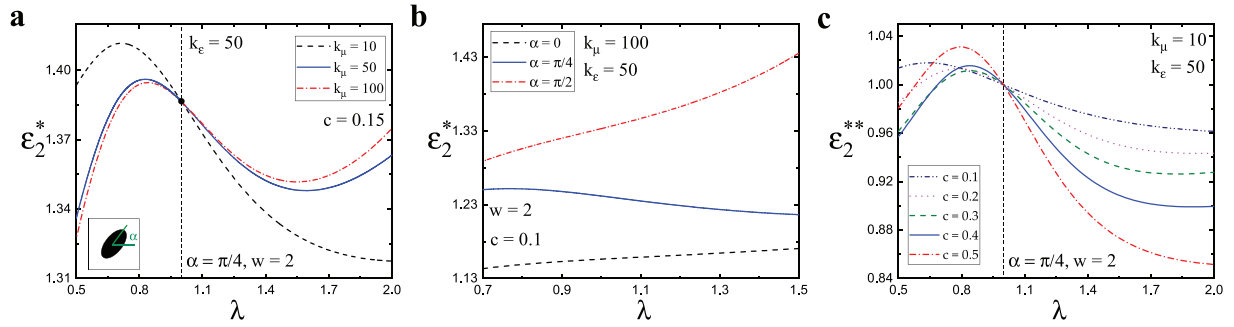


**Fig. 5.** Effective permittivity vs stretch for periodic DE composite with an elliptical inclusion with different contrasts in the shear moduli (a), inclination angles (b) and volume fractions of the elliptical inclusion (c). The contrast in the relative permittivities is  $k_\epsilon = 50$ . The aspect ratio of the elliptical inclusion is  $w = 2$ . (a) Black dashed, blue continuous and red dash-dotted curves are for DE composites with the shear moduli contrasts  $k_\mu = 10, 50, 100$ , respectively; the inclination angle  $\alpha = \pi/4$  and volume fraction  $c = 0.15$  are fixed. (b) Black dashed, blue continuous and red dash-dotted curves are for the composites with the initial inclination angles  $\alpha = 0, \pi/4$  and  $\pi/2$ , respectively; the volume fraction  $c = 0.1$  and shear modulus contrast  $k_\mu = 100$  are fixed. (c) Black dash-dot-dotted, magenta dotted, green dashed, blue continuous, red dash-dotted curves are for the composites with volume fractions  $c = 0.1, 0.2, 0.3, 0.4$  and  $0.5$ , respectively; the shear modulus contrast  $k_\mu = 10$  and initial inclination angle  $\alpha = \pi/4$  are fixed. (For interpretation of the references to color in this figure legend, the reader is referred to the web version of this article.)

of inclusion angle  $\alpha$  is  $\Delta_\epsilon = [(\epsilon_2^*|_{\alpha=\pi/2} - \epsilon_2^*|_{\alpha=0})/\epsilon_2^*|_{\alpha=0}] \cdot 100\% = 15.33\%$ , without any deformation ( $\lambda = 1$ ). Furthermore, we can achieve additional tunability of  $\epsilon_2^*$  with applied deformation. For example, for DE composite with  $\alpha = \pi/2$ , the change in  $\epsilon_2^*$  because of deformation is  $\Delta_\epsilon = [(\epsilon_2^*|_{\lambda=1.5} - \epsilon_2^*|_{\lambda=0.7})/\epsilon_2^*|_{\lambda=0.7}] \cdot 100\% = 11.36\%$ .

The dependence of the normalized effective permittivity on the applied stretch for inclusion volume fractions  $c = 0.1$  (navy dash-dot-dotted curve),  $c = 0.2$  (magenta dotted curve),  $c = 0.3$  (olive dashed curve),  $c = 0.4$  (blue continuous curve) and  $c = 0.5$  (red dash-dotted curve) is shown in Fig. 5(c). The curves intersect at the point  $\lambda = 1$  since we normalize the effective permittivity by their initial value in the undeformed state  $\epsilon_2^{**}(\lambda) = \epsilon_2^*(\lambda)/\epsilon_2^*(\lambda = 1)$ . Consistent with the previous observations, we find that for compression ( $\lambda < 1$ ) each curve has its own maximum. The largest value of  $\epsilon_2^{**} = 1.031$  corresponds to the highest volume fraction  $c = 0.5$ . For tension ( $\lambda > 1$ ) we find that normalized effective permittivity decreases with the applied stretch. However, some local minima are observed for volume fractions  $c = 0.2$ ,  $\epsilon_2^{**} = 0.943$  at  $\lambda = 1.92$ ;  $c = 0.3$ ,  $\epsilon_2^{**} = 0.926$  at  $\lambda = 1.92$  and  $c = 0.4$ ,  $\epsilon_2^{**} = 0.899$  at  $\lambda = 1.9$ . An increase in the volume fraction leads to a decrease in the value of  $\epsilon_2^{**}$  for each value of the applied deformation.

#### 4.1.3. Two circular inclusions

Next, we examine the influence of the distance between the particles on the overall performance of DE composites. To this end, we consider the periodic DE composites with two circular particles in a unit cell illustrated in Fig. 2(d). The normalized diameter of the inclusions is  $d_0 = d_a/a = 0.07$  and the distance between the particle centers is denoted by  $d$ . We define the orientation angle  $\theta$  as the angle between the line connecting two particle centers and vector  $\mathbf{e}_2$ . Here we illustrate the performance of the DE composites on the example of a particular system with the permittivity contrast  $k_\epsilon = 200$  in the undeformed state.

Fig. 6 shows the effective permittivity as functions of the dimensionless parameter  $s = (d - d_0)/d_0$  for orientation angles  $\theta = 0^\circ, 30^\circ, 45^\circ, 55^\circ, 60^\circ, 70^\circ$ , and  $90^\circ$  degrees, as annotated. The horizontal dashed line corresponds to the single inclusion case (see Fig. 2(b)) with diameter  $\sqrt{2}d_0$ , so the particle volume fraction equals to the volume fraction of two equi-sized particles with diameter  $d_0$ . As expected, the highest and the lowest values of the effective permittivity is found in the DE composites with  $\theta = 0^\circ$  and  $90^\circ$  degrees. An increase in the orientation angle leads to a decrease in the effective permittivity for each value of  $s$ . For all values of  $\theta$  the effective permittivity is a monotonically decreasing function of  $s$ , except for  $55^\circ$  and  $60^\circ$  cases possessing their local minimum. We observe that the difference between the curves increases significantly as inter-particle distance  $d$  (or  $s$ ) becomes relatively small. As the distance between two particles is increased, the two-particle system

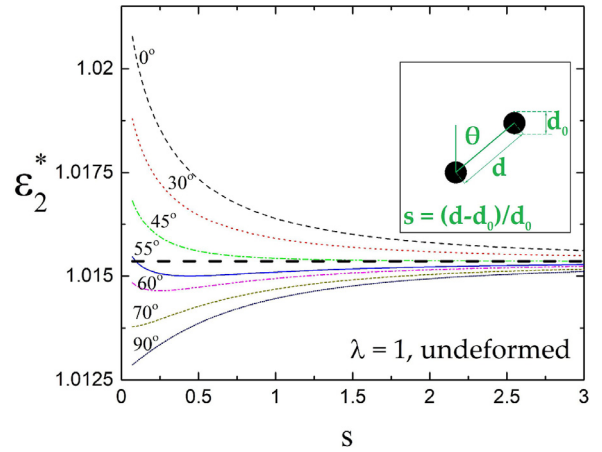


**Fig. 6.** Effective permittivity vs distance between two circular particles in the undeformed state  $\lambda = 1$ . The diameter of inclusions is  $d_0 = 0.07$ . The contrast in the relative permittivities is  $k_\epsilon = 200$ . Black dashed, red dotted, green dash-dotted, blue continuous, magenta dash-dot-dotted, dark yellow short-dashed and navy short dotted curves correspond to orientation angles  $\theta = 0^\circ, 30^\circ, 45^\circ, 55^\circ, 60^\circ, 70^\circ$ , and  $90^\circ$ , respectively. The horizontal dashed line denotes the effective permittivity for a single particle unit cell with diameter  $\sqrt{2}d_0$ . (For interpretation of the references to color in this figure legend, the reader is referred to the web version of this article.)

approaches the behavior similar to the single particle case. Therefore, the curves in Fig. 6 gradually approach the horizontal dashed line corresponding to the effective permittivity value of the single particle unit cell. Here, we observe no significant changes in the values of permittivity for distances larger than  $s \approx 2$ .

#### 4.1.4. Multi-particle microstructures with random distributions of inclusions

In this section, we study the effective permittivity of isotropic DE composites with randomly and uniformly distributed circular equi-sized particles. The distribution of the particles in the unit cell was generated by using the random adsorption algorithm [63] (additional details are provided in Appendix B). To avoid mesh distortion, the distances between inclusions were set such that it does not exceed the value of  $0.05d$ . The shear modulus contrast is  $k_\mu = 100$  and the volume fraction of the inclusion phase is  $c = 0.1$ . Examples of the considered representative 2-D unit cells with the number of particles  $N = 3, 5, 20$ , and  $50$  are shown in Fig. 7.

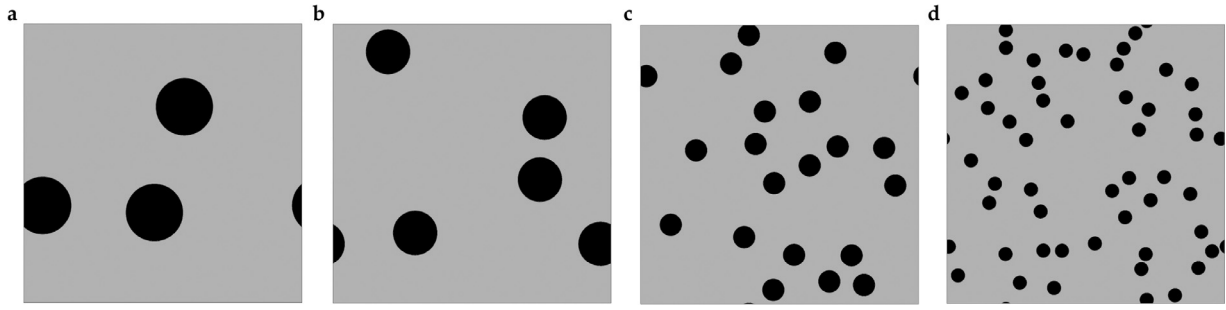


Fig. 7. Schematic representation of DE composites with randomly distributed particles. The volume fraction of the inclusion phase is  $c = 0.1$ . Five periodic unit cells are presented for the number of particles  $N = 3$  (a), 5 (b), 20 (c), and 50 (d).

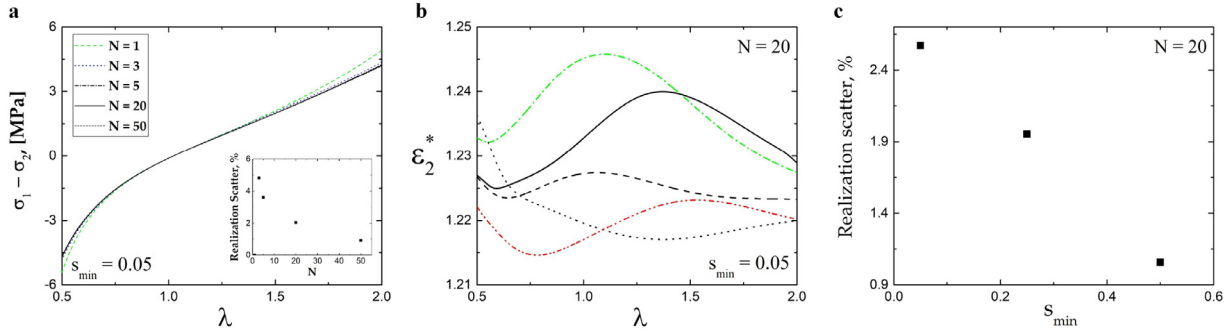


Fig. 8. (a) Cauchy stress vs stretch ratio for periodic composites with various numbers of particles in the periodic unit cell from  $N = 1$  to  $N = 50$ . The inset in (a) shows the realization scatter of the Cauchy stress for  $N = 3, 5, 20, 50$  particles. (b) The effective permittivity vs stretch ratio for five different realizations for the number of particles  $N = 20$ . (c) Realization scatter of the effective permittivity-stretch response for  $N = 20$  particles in the unit cell as a function of the minimum allowed distance between the particles. The contrasts in the shear moduli is  $k_\mu = 100$  and relative permittivities is  $k_\epsilon = 200$ , respectively. The volume fraction of the inclusion phase is  $c = 0.1$ . Realization scatter defined as  $(\epsilon_{\max} - \epsilon_{\min})/\epsilon_{\min}$  across 5 realizations of the composite with fixed number of particles  $N$ . The minimum distance between the particles is set to  $0.05d_0$  ( $s_{\min} = 0.05$ ).

First, we illustrate the influence of the number of particles included in a unit cell on the overall response of the DE composite. This also illustrates the transition in the composite behavior from periodic to a randomly distributed one. We consider the DE composites with four different particle numbers  $N = 3, 5, 20, 50$ . Five different realizations for each case are calculated and averaged. The average Cauchy stress normal components  $(\sigma_{11} - \sigma_{22})$  for five realizations of each  $N$  are shown in Fig. 8(a) as functions of the applied strain. The green-dashed curve, for  $N = 1$ , corresponds to the structure shown in Fig. 2(b) and is given here as a reference. The normalized applied electric field is  $\hat{E}_2^0 = 0.665$ . We observe that the average normal Cauchy stress increases as the applied deformation increases. We find that the responses of the composites with the number of particles  $N = 5, 20$ , and  $N = 50$  are almost indistinguishable from each other. The inset in Fig. 8(a) represents the realization scatter (here, by the realization scatter we mean the difference between maximum and minimum values among five realizations for a composite with a fixed number of particles) for various  $N$ . Note that the realization scatter of the single particle unit cell  $N = 1$  is zero. As expected, the realization scatter decreases with an increase in the particle number  $N$ . Thus, the dependence of the Cauchy stress on the applied deformation converges (i.e., becomes insensitive of the realization) for higher  $N$ .

In Fig. 8(b), we consider the effect of the applied deformation on the effective permittivity for five different realizations of the unit cell with  $N = 20$  particles. These different realization are denoted by green dash-dotted, blue continuous, black dashed, magenta dotted and red dash-dot-dotted curves. We observe that the effective permittivity of the five composites is characterized by some different values<sup>1</sup> even for the undeformed case  $\lambda = 1$ . We note that the difference in these values is in-

significant compared to the permittivity contrast used here ( $k_\epsilon = 200$ ). We conclude that the applied deformation barely influences the effective permittivity in DE composites with a random particle distribution. The influence of the applied deformation on the effective permittivity is comparable to the fluctuations observed in the undeformed case.

In Section 4.1.3, we illustrated that the inter-particle distance greatly affects the permittivity of the DE composites. Motivated by this observation, we investigate how the realization scatter of the effective permittivity in Fig. 8(b) is affected by the distance between particles. Fig. 8(c) summarizes the results showing the realization scatter as a function of the minimum allowed distance between the particles  $s_{\min}$  for the DE composite with the number of particles  $N = 20$ . In agreement with the previous observations for the two-particle system (Section 4.1.2), we report that the effective permittivity is highly sensitive to changes in inter-particle distance, as well as to changes in their positions relatively to the applied electric field (orientation angle). The realization scatter decreases fast (resembling the behavior of the curves in Fig. 6) as the distance between inclusions increases.

For completeness, we show the distribution of the local electric field magnitude  $|\hat{E}|/|\hat{E}_2^0| = \sqrt{\hat{E}_1^2 + \hat{E}_2^2}/\hat{E}_2^0$  inside the undeformed unit cell in Fig. 9. The three unit cells are shown for  $s_{\min} = 0.05, 0.25$  and  $0.5$ . The normalized applied electric field is  $\hat{E}_2^0 = 0.665$ . We observe high concentrations of the electric field (red colors) in the regions where the particles are very close to each other (we note the similarity with the different physical phenomena in the thermal and elastic granular media reported in [64]) or in the regions with chain-like particle structures in the direction of the vertically applied electric field. An increase in the distance between particles results in a more uniform distribution of the electric field outside the particles: dark-red colors (used for the regions with high concentrations of the electric field) for  $s_{\min} = 0.05$  change to light-red for  $s_{\min} = 0.25$  or even orange colors for the case of  $s_{\min} = 0.5$ .

<sup>1</sup> This effect was also observed even for higher number of particles such as  $N = 200$  and  $N = 500$

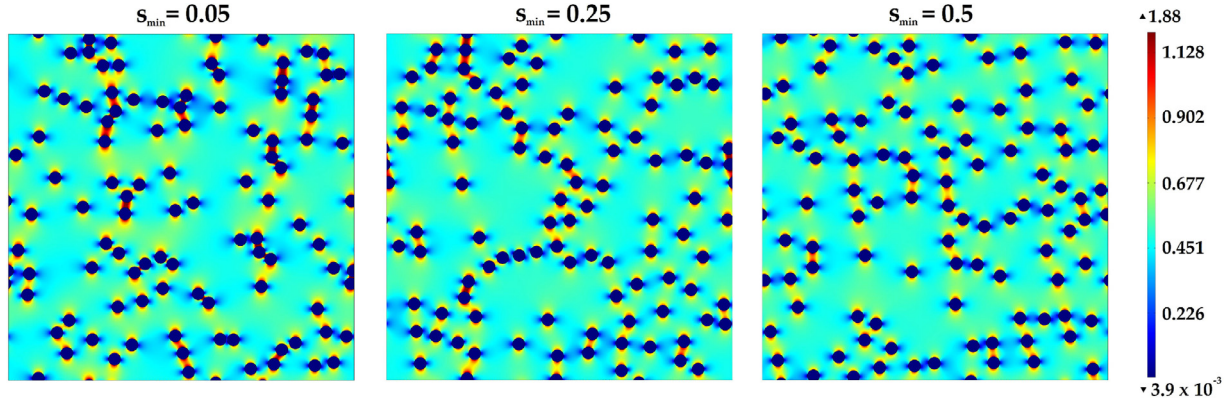


Fig. 9. The distribution of the local electric field magnitude  $|\hat{\mathbf{E}}|/|\hat{\mathbf{E}}_2|$  in the various realizations of the undeformed ( $\lambda = 1$ ) unit cell with different minimum distances between inclusions in each realization  $s_{\min} = 0.05$  (left),  $s_{\min} = 0.25$  (center) and  $s_{\min} = 0.5$  (right). The contrast in the relative permittivities is  $k_\epsilon = 200$ . The volume fraction of the inclusion phase is  $c = 0.1$ . The particle number is  $N = 100$ . The color bar indicates the electric field magnitude. The normalized applied electric field level is  $|\hat{\mathbf{E}}_2| = 0.665$ . (For interpretation of the references to color in this figure legend, the reader is referred to the web version of this article.)

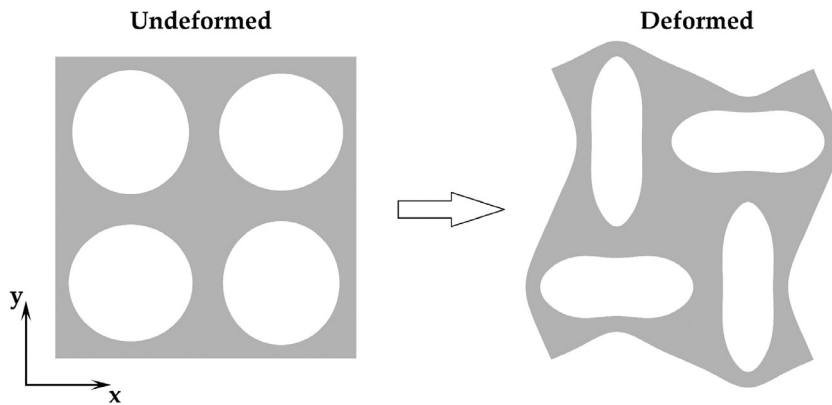


Fig. 10. Schematic representation of the instability-induced microstructural transformation. DE composite with periodically distributed circular voids in the undeformed (left) and buckled configuration (right). The volume fraction of the voids is  $c = 0.5$ . The applied compressive deformation is  $\lambda = 0.85$ .

#### 4.2. Periodic composites with instability-induced microstructure transformations

In this section, we study the permittivity tunability in the DE periodic systems experiencing *buckling-induced microstructure transformations*. First, we employ the instability phenomenon for permittivity tunability in the DE periodic void-matrix material [54]. This soft periodic system undergoes considerable buckling-induced microstructure transformations upon exceeding the critical deformation level. In particular, upon the onset of instabilities, the voids suddenly collapse, leading to the periodicity doubling and significant changes in the microstructure (see the schematic representation of the composite in Fig. 10).

In our modeling, the soft matrix is described by the ideal dielectric elastomer model as defined in Eq. (15); the voids are characterized by zero mechanical energy and permittivity equaled to that of the free space. To capture the postbuckling behavior, we consider a periodic unit cell with slightly perturbed shape of voids<sup>2</sup> (as shown in Fig. 10).

The dependence of the normalized effective permittivity on the applied stretch for the DE composites with the void volume fractions  $c = 0.5$  (red dash-dotted curve), 0.55 (blue continuous curve), and 0.6 (black dashed curve) is shown in Fig. 11(a). The critical points are denoted by circles. The critical stretch ratio  $\lambda_c$  increases with an increase in the volume fraction of the void from  $\lambda_c = 0.933$  for  $c = 0.5$  to  $\lambda_c = 0.955$  for  $c = 0.55$ , and  $\lambda_c = 0.973$  for  $c = 0.6$  (recall that  $\lambda_c = 0.933$  corresponds to higher applied deformation than  $\lambda_c = 0.973$ ). We observe that the ef-

fective permittivity increases monotonically with an increase in the applied compression level. This is mostly due to the fact that the void volume decreases as the material is compressed. To illustrate that, in Fig. 11(b), we plot the effective matrix volume fraction  $c_{eff}^{(m)}$  as the function of applied stretch  $\lambda$ . Clearly, as the compression level is increased ( $\lambda$  is decreased), the effective matrix volume fraction increases, thus, leading to an increase in the effective permittivity.

We note that the rate of change in  $c_{eff}^{(m)}$  with the applied deformation (slope of curves in Fig. 11(b)) increases after the onset of instability. Interestingly, the onset of instabilities, and subsequent microstructure transformation, barely affects the increase rate (or the slope of the curves in Fig. 11(a)) in effective permittivity with the applied deformation. The instability-induced microstructure transformation is accompanied by a change in the electric and electric displacement field distributions, illustrated in Fig. 11(c) and (d), respectively. The initial periodic array of circular voids transforms into an array of two vertically and two horizontally oriented elliptical shapes. This, in turn, leads to two competing effects: the one leading to effectively an increase in the permittivity of the voids which are horizontally oriented; and the competing one causing the decrease in effective permittivity of vertically oriented voids. To illustrate that, we show the distribution of the local electric field magnitude  $|\hat{\mathbf{E}}|/|\hat{\mathbf{E}}_2| = \sqrt{\hat{E}_1^2 + \hat{E}_2^2}/\hat{E}_2^0$  (see Fig. 11(c)) and electric displacement field magnitude  $|\hat{\mathbf{D}}|/|\hat{\mathbf{D}}_2| = \sqrt{\hat{D}_1^2 + \hat{D}_2^2}/\hat{D}_2^0$  (see Fig. 11(d)) inside the buckled unit cell at  $\lambda = 0.85$ . The normalized applied electric field is  $\hat{E}_2^0 = 0.02$  with  $\hat{D}_2^0 = \epsilon_0 \hat{E}_2^0$ . We observe that the distribution of the fields inside the voids is almost homogeneous, but their magnitudes are dependent on the orientation of voids. Specifically, the magnitude of the fields inside the horizontally oriented voids is approximately twice

<sup>2</sup> We imposed the imperfection by using elliptic voids with very small aspect ratio 1.001:1. It was verified that the geometrical imperfection does not affect the predicted critical stretches or the instability-induced patterns.

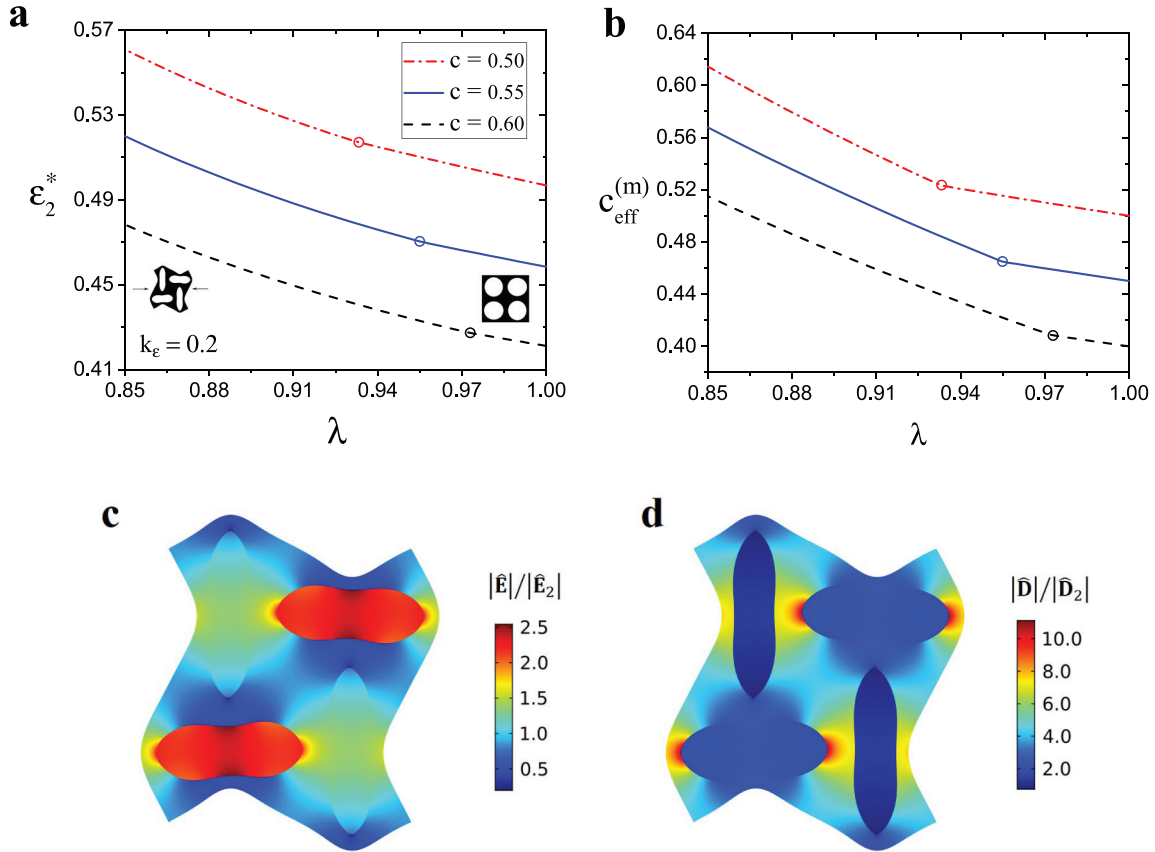


**Fig. 11.** (a) Effective permittivity  $\epsilon_2^*$  and (b) effective matrix volume fraction  $c_{eff}^{(m)}$  vs applied stretch  $\lambda$  for DE composites with different volume fractions of the void phase. Black dashed, blue continuous, and red dash-dotted curves correspond to volume fractions  $c = 0.5, 0.55$ , and  $0.6$ , respectively. The distribution of the local electric field magnitude  $|\hat{\mathbf{E}}|/|\hat{\mathbf{E}}_2|$  (c), and electric displacement field magnitude  $|\hat{\mathbf{D}}|/|\hat{\mathbf{D}}_2|$  (d) inside the buckled DE composite. The applied electric field is  $|\hat{\mathbf{E}}_2| = 0.02$  and  $|\hat{\mathbf{D}}_2| = \epsilon_0|\hat{\mathbf{E}}_2|$ . (For interpretation of the references to color in this figure legend, the reader is referred to the web version of this article.)

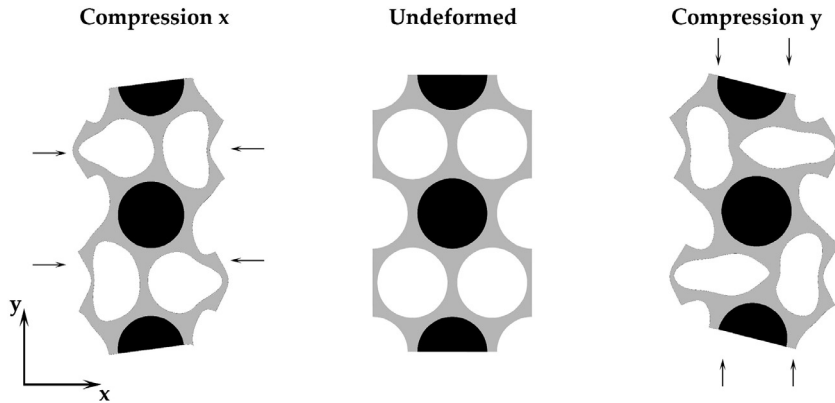


**Fig. 12.** Schematic representation of the instability-induced microstructural transformations in a soft porous material with periodically distributed voids. The applied compressive deformation in  $x$  (left) and  $y$  (right) directions is  $\lambda = 0.9$  and undeformed case  $\lambda = 1$  (center). The volume fractions of the matrix, voids and inclusions are  $c^{(m)} = 0.3, c^{(v)} = 0.525$  and  $c^{(i)} = 0.175$ .

of their magnitudes in vertically oriented voids. However, the distribution of the fields in the matrix is highly inhomogeneous, especially, in the region close to the voids. The highest and the lowest values of both the fields inside the matrix are observed near the horizontally and vertically oriented voids, respectively.

Next, we consider the DE composite comprising of the soft matrix, voids, and stiff inclusions with high permittivity [56–58]. Schematic representation of the composite is shown in Fig. 12. Similarly to the previously discussed periodic porous materials, the void-matrix-inclusion system also exhibit instabilities once a critical compressive deformation is exceeded. Similarly to the previous case, upon the onset of instabilities, the voids collapse co-operatively, and the composite structure

doubles the periodicity. However, the void-matrix-inclusion composites develop distinct deformation patterns due to the constraining stiff inclusions that regulate the onset of instabilities and the post-buckling behavior [57].

We consider the periodic unit cell with the width and height,  $a = 2$  and  $b = 2\sqrt{3}$ , respectively. The examples are given for the composite with volume fractions of the matrix, voids and inclusions are  $c^{(m)} = 0.3, c^{(v)} = 0.525$  and  $c^{(i)} = 0.175$ , respectively. The shear moduli and permittivities of the soft matrix are  $\mu^{(m)} = 0.2$  MPa and  $\epsilon^{(m)} = 6.5$  (corresponding to VHB 4910), and of the active inclusions are  $\mu^{(i)} = 2.7$  GPa and  $\epsilon^{(i)} = 6500$  corresponding to Polyaniline (PANI).



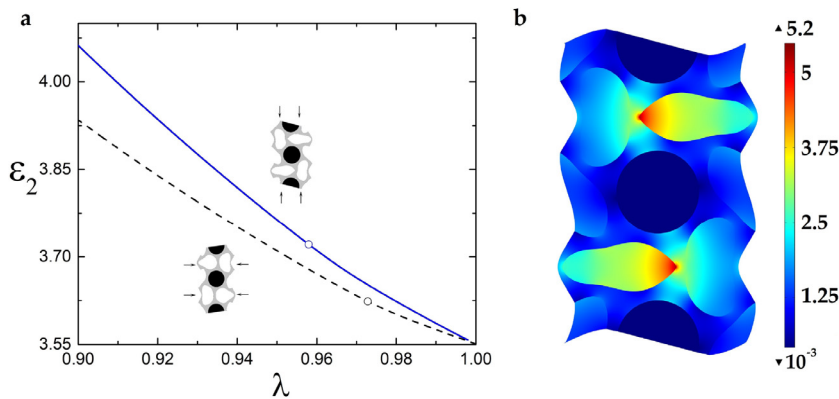


**Fig. 13.** (a) Permittivity vs stretch for the VHB 4910 with Polyaniline electroactive inclusions and voids. Black dashed and blue continuous curves correspond to compression  $x$  and compression  $y$ , respectively. (b) The distribution of the local electric field magnitude  $|\hat{\mathbf{E}}|/|\hat{\mathbf{E}}_2|$  inside the postbuckling compression  $y$  DE composite. The normalized applied electric field is  $|\hat{\mathbf{E}}_2| = 0.01$ . (For interpretation of the references to color in this figure legend, the reader is referred to the web version of this article.)

The dependence of the effective permittivity on the applied stretch is shown in Fig. 13(a). The critical points ( $\lambda_c = 0.973$  for compression  $x$  and  $\lambda_c = 0.958$  for compression  $y$ ) are denoted by circles. Consistently with the previous observations for homogeneous DE with voids, we find that the composite permittivity increases with an increase in the applied stretch for both compression  $x$  and  $y$ . The tunability of the permittivity, however, is higher for the case of compression  $y$ . For example, at the applied deformation of  $\lambda = 0.9$  the change of the permittivity is 14.4% for compression  $y$  and 10.7% for compression  $x$ .

We note that the effective permittivity is very sensitive to the distance between electroactive inclusions (see Section 4.1.3) which is greatly affected if the compression is applied in the  $y$  direction. On the other hand, the permittivity also depends on the position of the electroactive inclusions with respect to the applied electric field (see Section 4.1.3). Because the vertical alignment of the electroactive inclusions (see Fig. 12) is not affected by buckling, the effect of the instability on the slope of the curves in Fig. 13(a) is relatively small. To investigate the effect, we examine the electric field distribution in the postbuckling configuration of the DE composite.

The distribution of the local electric field magnitude  $|\hat{\mathbf{E}}|/|\hat{\mathbf{E}}_2| = \sqrt{\hat{E}_1^2 + \hat{E}_2^2}/\hat{E}_2^0$  is shown in Fig. 13(b). The normalized applied electric field is  $\hat{E}_2^0 = 0.01$ . We observe that electric field is homogeneous inside the electroactive inclusions and has the lowest value because the permittivity of the PANI  $\epsilon^{(i)} = 6500$  is much higher than of the VHB  $\epsilon^{(m)} = 6.5$  and voids  $\epsilon^{(v)} = 1$ . The highest values of the electric field are in the region between electroactive inclusions. In addition, we observe the high inhomogeneity of the electric field near the edges of the voids between inclusions.

## 5. Conclusions

In this work, we investigated the behavior of finitely strained DE composites with periodic and random distributions of inclusions. We analyzed the influence of the mechanical pre-stretch, geometrical and material parameters on the effective permittivity of the DE composites with particulate microstructures. For periodically distributed circular inclusions, we found that tunability of the effective permittivity increases with an increase in the shear moduli contrast. In particular, we found that deformations up to 100%, for a relatively small volume fraction of the electroactive phase  $c = 0.15$ , can cause changes in the permittivity more than 30%. An explicit expression for the effective permittivity as a function of the applied deformation was derived under the assumption of rigid (or negligibly deformed) inclusions. For elliptical inclusions, we found that the orientation angle significantly affects the effective permittivity. An increase in the inclination angle results in rapid increase in the effective permittivity. The highest permittivity was observed when the major semi-axis of elliptical inclusion is parallel to the applied electric field and the lowest one was found for the case of the major semi-axis forming a normal angle with the applied electric field; this is always ob-

served regardless of the applied pre-strain. The applied deformation and the orientation angle variations can cause changes in the overall permittivity of more than 25% even for a relatively small volume fraction of the electroactive phase ( $c = 0.1$ ). For the case of randomly distributed stiff inclusions, we found that the Cauchy stress–stretch dependence is barely altered by the number of particles in the unit cell for  $N > 20$ . Thus, the mechanical aspect of the DE composite behavior can be modelled accurately enough by considering a representative volume element (RVE) with  $N = 20$  particles in the unit cell. The effective permittivity of random mixtures was found to be minimally affected by deformation. However, small variations in effective permittivity were observed between different particle placement realizations of the RVE, even with identical numbers of particles. This variation can be explained by examining the behavior of a two particle periodic systems. We found that, in this system, geometric parameters such as orientation angle and distance between the two particles, significantly affected the relative permittivity. This, however, happens only if the particles are closer than twice the particle diameter. As a result, the variation in permittivity between realizations of the RVE significantly decreases as the interparticle distance increases. We also observed high electromechanical stresses in the regions where the particles are close to each other, and in the regions with chain-like particle structures. The electromechanical stresses in these regions increased significantly when the minimum distance between the particles was decreased from  $0.5d$  to  $0.05d$ . Such high stresses could potentially lead to debonding of the particles from the matrix, resulting in an overall decrease in the electromechanical coupling, degradation of the matrix, and, potentially, leading to electromechanical instabilities [65–69].

Finally, we explored the permittivity tunability in DEs with periodically distributed voids and inclusions. In these systems the effective permittivity increases with applied compression. While the tunability of the effective permittivity was found to be significant, the onset of buckling, however, did not change the dependence of the permittivity on the applied deformation. Collectively, these results illustrate the potential of porous DEs to function as stretch sensors and self-tuning dielectric substrates in potential applications of wearable electronics, soft robotics and flexible antennas, and motivate further experimental and theoretical investigation of this electromechanical tuning mechanism.

## Author Statement

Artemii Goshkoderia, Viacheslav Slesarenko, Jian Li, and Nitesh Arora contributed to the numerical and analytical model development and producing the results, Philip Buskohl, Abigail Juhl and Vincent Chen, and Stephan Rudykh discussed the research, developed the idea, and oversaw the research. All authors participated in the manuscript composition and discussion.

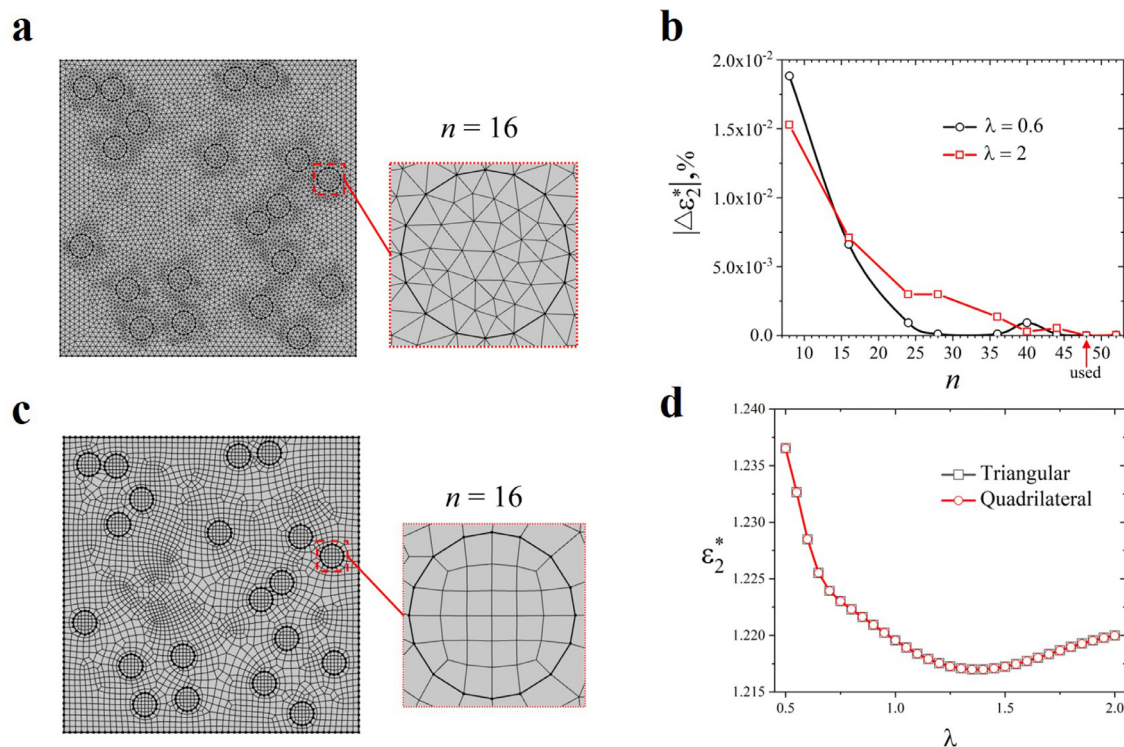


**Fig. A1.** The representative volume elements discretized using triangular (a), and quadrilateral (c) elements with  $n = 16$ . Percentage relative difference in effective permittivity  $|\Delta \epsilon_2^*|, \%$  vs. the number of elements at the inclusion boundary  $n$  (b). Effective permittivity  $\epsilon_2^*$  vs. stretch ratio  $\lambda$  for mesh with triangular (black squares) and quadrilateral (red circles) elements (d). (For interpretation of the references to color in this figure legend, the reader is referred to the web version of this article.)

### Declaration of Competing Interest

The authors declare that they have no known competing financial interests or personal relationships that could have appeared to influence the work reported in this paper.

### Acknowledgments

The research was partially supported by Grainger Institute for Engineering, by the University of Wisconsin - Madison Office of the Vice Chancellor for Research and Graduate Education with funding from the Wisconsin Alumni Research Foundation, and by the [Air Force Office of Scientific Research](#) under the research tasks [17RXCOR435](#) and [FA8655-20-1-7003](#) though Project No. 19IOE010. VS acknowledges the support of the EU through [Marie-Sklodowska-Curie](#) grant agreement No [754340](#) and the Deutsche Forschungsgemeinschaft (DFG, [German Research Foundation](#)) under Germany's Excellence Strategy [EXC-2193/1 390951807](#).

### Appendix A. Finite element mesh sensitivity analysis

To ensure the accuracy of the numerical results, we perform the mesh sensitivity analysis. To illustrate the analysis, we show the results for the DE composite with a multi-particle microstructure with random distributions of  $N = 20$  inclusions. Fig. A.14(a) and (c) show the representative unit cells with triangular and quadrilateral mesh elements, respectively. We prescribe the number of elements on the boundary of each inclusions  $n$ , as illustrated in the insets of Fig. A.14(a) and (c). In the shown meshes, the prescribed number of elements on each inclusion boundary is  $n = 16$ . Clearly, the total number of elements in the unit cell is also dictated by the value of  $n$ . For example, the total number of elements increases from 6767 to 25,130 as the inclusion boundary element number is increased from  $n = 8$  to  $n = 48$ . Fig. A.14(c) shows the relative difference in the effective permittivity (in percent) versus the controlled

inclusion boundary element number. The relative difference in the effective permittivity is defined as  $|\Delta \epsilon_2^*| = |(\epsilon_n - \epsilon_{conv}) / \epsilon_{conv}|$ , where  $\epsilon_n$  is the value of  $\epsilon_2^*$  obtained using a mesh with  $n$  elements on the inclusion boundary, while  $\epsilon_{conv}$  denotes the converged value of  $\epsilon_2^*$ , with  $n = 48$ . The examples of the dependence are shown for the large stretch levels, namely,  $\lambda = 0.6$  (black circles) and  $\lambda = 2$  (red squares). While the difference in the obtained values is extremely small – less than 0.02% even for  $n = 8$ , it rapidly decreases even lower as  $n$  is further increased. We note that we used the meshes with  $n = 48$  elements on the boundary of each circular inclusion (marked as “used” in Fig A.14(b)) to ensure a sufficient accuracy level of the calculations.

For completeness, we show a comparison of the results for the DE composite unit cell discretized by using quadrilateral elements (as shown in Fig. A.14(c)). Fig. A.14(d) shows the effective permittivity  $\epsilon_2^*$  as a function of stretch ratio  $\lambda$  calculated using the mesh with triangular (black squares) and quadrilateral (red circles) elements. Note that both meshes were generated while using the identical number of inclusion boundary elements, namely,  $n = 48$ . We observe that these calculation produced identical results for the whole range of the considered deformations.

### Appendix B. Random adsorption algorithm

In this work, the distribution of inclusions in DE composite with multi-particle microstructure is performed using the so-called random sequential adsorption (RSA) algorithm [63]. The algorithm is based on the sequential addition of the inclusions into the unit cell. Each new particle is assigned a random position of its center and attempted to be placed into the unit cell. Particle placement is successful only if the distances between its center and the centers of already placed inclusions exceed  $d + \epsilon$ . If the center-to-center distance is less than  $d + \epsilon$ , the candidate is discarded, and a new placement is attempted. Here,  $d$  is the diameter of the circular inclusions, and  $\epsilon$  is the inter-particle minimum distance, which is typically used to avoid inadequately fine mesh be-

two inclusions. Here, we assign  $\varepsilon = 0.05d$ , and used the same value to prohibit the center of the candidate inclusion from locating within  $\left[\frac{d}{2} - \frac{\varepsilon}{2}, \frac{d}{2} + \frac{\varepsilon}{2}\right]$  range from the boundaries of the unit cell, thus avoiding mesh distortion. RSA enables a fast and efficient way of randomly filling the area for relatively low volume fractions of inclusions. In particular, for 2D circular disks within the square unit cell, the algorithm works well for volume fraction  $c \lesssim 0.3$ , and achieves the saturation for  $c \approx 0.547$  [70], which is lower than the theoretical packing limit of 0.9069 [71,72]. For high and moderate volume fractions, more sophisticated packing algorithms are recommended to be used [73,74]. By employing RSA we generated the representative volume elements with inclusion volume fraction  $c = 0.1$ . Examples of the considered representative 2-D unit cells with the number of particles  $N = 3, 5, 20$  and 50 are shown in Fig. 7.

## References

- Pelrine RE, Kornbluh RD, Joseph JP. Electrostriction of polymer dielectrics with compliant electrodes as a mean of actuation. *Sens Actuators A* 1998;64:77–85.
- Pelrine R, Kornbluh R, Pei Q-B, Joseph J. High-speed electrically actuated elastomers with strain greater than 100%. *Science* 2000;287:836–9.
- Pelrine R, Kornbluh R, Joseph J, Heydt R, Pei Q-B, Chiba A. High-field deformation of elastomeric dielectrics for actuators. *Mater Sci Eng* 2000;11:89–100.
- Mao G, Wu L, Fu Y, Chen Z, Natani S, Gou Z, et al. Design and characterization of a soft dielectric elastomer peristaltic pump driven by electromechanical load. *IEEE/ASME Trans Mechatron* 2018;23:2132–43.
- Bar-Cohen Y. EAP history, current status, and infrastructure. In: Bar-Cohen Y, editor. *Electroactive Polymer (EAP) actuators as artificial muscles*. Bellingham, WA: SPIE press; 2001. p. 3–44.
- Kornbluh RD, Pelrine R, Prahald H, Wong-Foy A, McCoy B, Kim S, Eckerle J, Low T. From boots to buoys: promises and challenges of dielectric elastomer energy harvesting. In: *Electroactivity in polymeric materials*. Springer; 2012. p. 67–93.
- McKay T, O'Brien B, Calius E, Anderson I. An integrated, self-priming dielectric elastomer generator. *Appl Phys Lett* 2010;97.
- Carpi F, Frediani G, Turco S, De Rossi D. Bioinspired tunable lens with muscle-like electroactive elastomers. *Adv Funct Mater* 2011;21:4152–8.
- Bortot E, Denzer R, Menzel A, Gei M. Analysis of viscoelastic soft dielectric elastomer generators operating in an electrical circuit. *Int J Solids Struct* 2016;78–79:205–15.
- Gei M, Roccabianca S, Bacca M. Controlling bandgap in electroactive polymer-based structures. *Mechatronics IEEE/ASME Trans* 2011;16:102–7.
- Galich P, Rudykh S. Manipulating pressure and shear elastic waves in dielectric elastomers via external electric stimuli. *Int J Solids Struct* 2016;91:18–25.
- Galich PI, Rudykh S. Shear wave propagation and band gaps in finitely deformed dielectric elastomer laminates: long wave estimates and exact solution. *J Appl Mech* 2017;84:91002.
- Jandron M, Henann DL. A numerical simulation capability for electroelastic wave propagation in dielectric elastomer composites: application to tunable soft phononic crystals. *Int J Solids Struct* 2018;150:1–21.
- Zhu J, Chen H, Wu B, Chen W, Balogun O. Tunable band gaps and transmission behavior of sh waves with oblique incident angle in periodic dielectric elastomer laminates. *Int J Mech Sci* 2018;146:81–90.
- Yin T, Wu T, Zhong D, Liu J, Liu X, Han Z, et al. Soft display using photonic crystals on dielectric elastomers. *ACS Appl Mater Interfaces* 2018;10:24758–66.
- Zhang QM, Li H, Poh M, Xia F, Cheng Z-Y, Xu H, Huang C. An all-organic composite actuator material with a high dielectric constant. *Nature* 2002;419:284–9.
- Huang C, Zhang QM. Enhanced dielectric and electromechanical responses in high dielectric constant all-polymer percolative composites. *Adv Funct Mater* 2004;14:501–6.
- Gei M, Springhetti R, Bortot E. Performance of soft dielectric laminated composites. *Smart Mater Struct* 2013;22:104014.
- Liu L, Kong L, Matitsine S. Tunable effective permittivity of carbon nanotube composites. *Appl Phys Lett* 2008;93:113106.
- Ouyang G, Wang K, Chen X. TiO<sub>2</sub> nanoparticles modified polydimethylsiloxane with fast response time and increased dielectric constant. *J Micromech Microeng* 2012;22:74002.
- Yang D, Tian M, Dong Y, Kang H, Gong D, Zhang L. A high-performance dielectric elastomer consisting of bio-based polyester elastomer and titanium dioxide powder. *J Appl Phys* 2013;114:154104.
- Huang X, Xie L, Hu Z, Jiang P. Influence of batio<sub>3</sub> nanoparticles on dielectric, thermophysical and mechanical properties of ethylene-vinyl acetate elastomer/batio<sub>3</sub> microcomposites. *IEEE Trans Dielectr Electr Insul* 2011;18:375–83.
- Bai Y, Cheng Z-Y, Bharti V, Xu H, Zhang Q. High-dielectric-constant ceramic-powder polymer composites. *Appl Phys Lett* 2000;76:3804–6.
- Rudykh S, Lewinstein A, Uner G, deBotton G. Analysis of microstructural induced enhancement of electromechanical coupling in soft dielectrics. *Appl Phys Lett* 2013;102:151905.
- Toupin RA. The elastic dielectric. *Arch Rational Mech Anal* 1956;5:849–915.
- Toupin RA. Stress tensors in elastic dielectrics. *Arch Ration Mech Anal* 1960;5:440–52.
- Dorfmann A, Ogden RW. Nonlinear electroelasticity. *Acta Mech* 2005;174:167–83.
- Keip M-A, Steinmann P, Schröder J. Two-scale computational homogenization of electro-elasticity at finite strains. *Comput Methods Appl Mech Eng* 2014;278:62–79.
- Vu D, Steinmann P. Nonlinear electro-and magneto-elastostatics: material and spatial settings. *Int J Solids Struct* 2007;44:7891–905.
- Cohen N. Enhancing the electro-mechanical response of stacked dielectric actuators. *J Elast* 2017;127:103–13.
- Jones SB, Friedman SP. Particle shape effects on the effective permittivity of anisotropic or isotropic media consisting of aligned or randomly oriented ellipsoidal particles. *Water Resour Res* 2000;36:2821–33.
- Rudykh S, Bhattacharya K, deBotton G. Snap-through actuation of thick-wall electroactive balloons. *Int J Nonlinear Mech* 2012;47:206–9.
- Keplinger C, Li T, Baumgartner R, Suo Z, Bauer S. Harnessing snap-through instability in soft dielectrics to achieve giant voltage-triggered deformation. *Soft Matter* 2012;8:285–8.
- Arora N, Kumar P, Joglekar MM. A modulated voltage waveform for enhancing the travel range of dielectric elastomer actuators. *J Appl Mech* 2018;85.
- Kolle M, Lethbridge A, Kreysing M, Baumberg J, Aizenberg J, Vukusic P. Bio-inspired band-gap tunable elastic optical multilayer fibers. *Adv Mater* 2013;25:2239–45.
- Lee H, Fang N. Micro 3d printing using a digital projector and its application in the study of soft materials mechanics. *J Vis Exp* 2012:e4457.
- Slesarenko V, Rudykh S. Harnessing viscoelasticity and instabilities for tuning wavy patterns in soft layered composites. *Soft Matter* 2016;12:3677–82.
- Wang Y, Sun L. Development of dielectric elastomer nanocomposites as stretchable actuating materials. *Appl Phys Lett* 2017;111:161904.
- Mazurek P., Skov A.L.. Novel high dielectric constant hybrid elastomers based on glycerol-insilicone emulsions. *IEEE; Dielectrics (ICD)*, 2016 IEEE international conference on, 1, 1–4.
- Wang J, Wang J-W, Zhou S-W, Wang G-Q, Zhang S. Approach to the fabrication of acrylic elastomer nanocomposites with high dielectric constants. *J Appl Polym Sci* 2016;133.
- Stoyanov H, Kollosche M, Risse S, McCarthy D, Kofod G. Elastic block copolymer nanocomposites with controlled interfacial interactions for artificial muscles with direct voltage control. *Soft Matter* 2011;7:194–202.
- Davies J, Miller R, Busse W. Dielectric properties of plasticized polyvinyl chloride. *J Am Chem Soc* 1941;63:361–9.
- Wissler M, Mazza E. Electromechanical coupling in dielectric elastomer actuators. *Sens Actuators, A* 2007;138:384–93.
- Jiménez SM, McMeeking RM. Deformation dependent dielectric permittivity and its effect on actuator performance and stability. *Int J Non Linear Mech* 2013;57:183–91.
- Jiménez SM, McMeeking RM. A constitutive law for dielectric elastomers subject to high levels of stretch during combined electrostatic and mechanical loading: elastomer stiffening and deformation dependent dielectric permittivity. *Int J Non Linear Mech* 2016;87:125–36.
- Itskov M, Khiêm VN, Waluyo S. Electroelasticity of dielectric elastomers based on molecular chain statistics. *Mathematics and Mechanics of Solids* 2018. 1081286518755846
- Mahanfar A, Menon C, Vaughan R, Carpi F, Parameswaran M, Daheshpour K. Tunable dielectric resonator antennas using voltage-controlled mechanical deformation. *Advances in Science and Technology* 2008;56:614–19. *Trans Tech Publ*
- Chang W-S, Yang C-F, Chang C-K, Liao W-J, Cho L, Chen WS. Pattern reconfigurable millimeter-wave antenna design for 5g handset applications. In: 2016 10th European conference on antennas and propagation (EuCAP); 2016. p. 1–3. *IEEE*
- Damm C, Maasch M, Gonzalo R, Jakoby R. Tunable composite right/left-handed leaky wave antenna based on a rectangular waveguide using liquid crystals. In: 2010 IEEE MTT-S international microwave symposium; 2010. p. 13–16. *IEEE*
- Liu L, Matitsine S, Tan P. Electromagnetic smart screen for tunable transmission applications. *Microscop Opt Technol Lett* 2008;50:1510–14.
- Lei KF, Lee K-F, Lee MY. Development of a flexible PDMs capacitive pressure sensor for plantar pressure measurement. *Microelectron Eng* 2012;99:1–5.
- Kollosche M, Stoyanov H, Laflamme S, Kofod G. Strongly enhanced sensitivity in elastic capacitive strain sensors. *J Mater Chem* 2011;21:8292–4.
- Zhang H, Wang MY, Li J, Zhu J. A soft compressive sensor using dielectric elastomers. *Smart Mater Struct* 2016;25:35045.
- Mullin T, Deschanel S, Bertoldi K, Boyce MC. Pattern transformation triggered by deformation. *Phys Rev Lett* 2007;99:84301.
- Li J, Pallicity TD, Slesarenko V, Goshkoderia A, Rudykh S. Domain formations and pattern transitions via instabilities in soft heterogeneous materials. *Adv Mater* 2019;31:1807309.
- Li J, Slesarenko V, Rudykh S. Auxetic multiphase soft composite material design through instabilities with application for acoustic metamaterials. *Soft Matter* 2018;14:6171–80.
- Li J, Rudykh S. Tunable microstructure transformations and auxetic behavior in 3d-printed multiphase composites: the role of inclusion distribution. *Composites Part B* 2019;172:352–62.
- Li J, Wang Y, Chen W, Wang Y-S, Bao R. Harnessing inclusions to tune post-buckling deformation and bandgaps of soft porous periodic structures. *J Sound Vib* 2019;459:114848.
- Dorfmann A, Ogden RW. Nonlinear electroelastostatics: incremental equations and stability. *Int J Eng Sci* 2010;48:1–14.
- Sihvola A, Lindell I. Polarizability modeling of heterogeneous media. *Progress in electromagnetics research (pier 6)*, dielectric properties of heterogeneous materials. Amsterdam: Elsevier; 1992.
- Kärkkäinen KK, Sihvola AH, Nikoskinen KI. Effective permittivity of mixtures: numerical validation by the fdtd method. *Geosci Remote Sens IEEE Trans* 2000;38:1303–8.

- [62] Hashin Z, Shtrikman S. A variational approach to the theory of the effective magnetic permeability of multiphase materials. *J Appl Phys* 1962;33:3125–31.
- [63] Segurado J, Llorca J. A numerical approximation to the elastic properties of sphere-reinforced composites. *J Mech Phys Solids* 2002;50:2107–21.
- [64] Willot F, Gillingibert L, Jeulin D. Microstructure-induced hotspots in the thermal and elastic responses of granular media. *Int J Solids Struct* 2013;50:1699–709.
- [65] Zurlo G, Destrade M, DeTommasi D, Puglisi G. Catastrophic thinning of dielectric elastomers. *Phys Rev Lett* 2017;118:78001.
- [66] Rudykh S, deBotton G. Stability of anisotropic electroactive polymers with application to layered media. *Z Angew Math Phys* 2011;62:1131–42.
- [67] Rudykh S, Bhattacharya K, deBotton G. Multiscale instabilities in soft heterogeneous dielectrics. *Proc R Soc A* 2014;470:20130618.
- [68] Goshkoderia A, Rudykh S. Electromechanical macroscopic instabilities in soft dielectric elastomer composites with periodic microstructures. *Eur J Mech-A/Solids* 2017;65:243–56.
- [69] Su Y, Wu B, Chen W, Destrade M. Finite bending and pattern evolution of the associated instability for a dielectric elastomer slab. *Int J Solids Struct* 2019;158:191–209.
- [70] Zhang G, Torquato S. Precise algorithm to generate random sequential addition of hard hyperspheres at saturation. *Phys Rev E* 2013;88:53312.
- [71] Conway JH, Sloane NJA. Sphere packings, lattices and groups. Springer Science & Business Media; 2013. 290
- [72] Tóth LF. Über gesättigte kreissysteme. *Math Nach* 1951;5:253–8.
- [73] Feng Y, Han K, Owen D. Filling domains with disks: an advancing front approach. *Int J Numer Methods Eng* 2003;56:699–713.
- [74] Ilin DN, Bernacki M. Advancing layer algorithm of dense ellipse packing for generating statistically equivalent polygonal structures. *Gran Matter* 2016;18:43.